

# Imaginary-time method for the radiative capture reaction rate

K. Yabana<sup>1,2,3</sup> and Y. Funaki<sup>2,3</sup>

<sup>1</sup>Center for Computational Sciences, University of Tsukuba, Tsukuba 305-8571, Japan

<sup>2</sup>Institute of Physics, University of Tsukuba, Tsukuba 305-8571, Japan

<sup>3</sup>Nishina Center for Accelerator-Based Science, The Institute of Physical and Chemical Research (RIKEN), Wako 351-0198, Japan

(Received 10 February 2012; published 14 May 2012)

We propose a new computational method for astrophysical reaction rate of the radiative capture process. In the method, an evolution of a wave function is calculated along the imaginary-time axis, which is identified as the inverse temperature. It enables direct evaluation of reaction rate as a function of temperature without solving any scattering problem. The method is tested for two-body radiative capture reaction,  $^{16}\text{O}(\alpha, \gamma)^{20}\text{Ne}$ , showing that it gives identical results to those calculated by the ordinary procedure. This method will be suited for calculation of triple- $\alpha$  radiative capture rate, for which an explicit construction of the scattering solution is difficult.

DOI: [10.1103/PhysRevC.85.055803](https://doi.org/10.1103/PhysRevC.85.055803)

PACS number(s): 26.20.-f, 24.10.-i, 25.40.Lw, 25.55.-e

## I. INTRODUCTION

Radiative capture reaction rate far below the Coulomb barrier is an essential input for quantitative understanding of stellar evolution and nucleosynthesis [1]. However, direct experimental measurements of relevant cross sections far below the Coulomb barrier often accompany difficulties because of their exponentially small cross sections. There are also a few three-body processes of significance for which experimental measurements are not feasible. Theoretical evaluation of the radiative capture reaction rate is thus important.

The radiative capture rate is composed of two distinct contributions, resonant and nonresonant processes. A potential model is often employed for the theoretical evaluation of the nonresonant capture rate. For two-body radiative capture processes, it is a routine procedure once the model potential is given. One first solves the radial Schrödinger equation (coupled-channel equation if necessary) under an appropriate scattering boundary condition to obtain scattering cross section. One then calculates the capture reaction rate as a function of temperature by integrating the cross section over the collision energy with an appropriate Boltzmann weight.

Theoretical evaluation of radiative capture reaction rate for three-body processes is a much more difficult problem. It is well recognized that the triple- $\alpha$  radiative capture reaction to form  $^{12}\text{C}$  is a key process to produce heavy elements [2]. At a temperature above 0.1 GK, a resonance state of  $0_2^+$  of  $^{12}\text{C}$ , which is known as the Hoyle state [3,4], contributes dominantly. Below 0.1 GK, on the other hand, nonresonant contribution is considered to be significant [5–7]. Recently, Ogata *et al.* [8] conducted a serious evaluation of the rate with the continuum-discretized coupled-channels (CDCC) method, a three-body reaction theory that has been successful for nuclear direct reactions [9,10]. The radiative capture rate reported by Ogata *et al.* was surprisingly large below 0.1 GK in comparison with the rate that has been employed in standard stellar-evolution calculations [1].

Theoretical evaluation of three-body radiative capture rate is accompanied by several difficulties. It is by no means obvious how to define theoretically the cross section of

the triple- $\alpha$  radiative capture process, because an analytic asymptotic form of the scattering wave function of three charged particles is not known. One also needs to solve the three-body problem in a huge spatial region for reactions far below the Coulomb barrier, since the  $\alpha$  particles pass through a barrier for a long distance to penetrate it.

In Ref. [11], de Diego *et al.* proposed an alternative procedure for the calculation of triple- $\alpha$  capture rate. They consider an inverse process, a photo-absorption of  $^{12}\text{C}$  in the excited  $2^+$  state, and calculate the transition probability in the bound-state approximation. This procedure allows one to avoid the difficulty of calculating scattering solution for three charged particles. However, a number of bound states need to be calculated in their approach.

In this paper, we propose a new computational method for the radiative capture rate. We show that the radiative capture rate as a function of temperature may be calculated directly by solving an equation that looks like a time-dependent Schrödinger equation along the imaginary-time axis. This method requires neither any solutions of scattering problem nor any bound-state solutions except for a final bound-state wave function after the capture. Since the method allows us to avoid the difficulties mentioned above, we believe it will be useful for the calculation of radiative capture rate of the triple- $\alpha$  process. In this paper, we demonstrate the feasibility of the method by applying it to two-body capture reaction,  $^{16}\text{O}(\alpha, \gamma)^{20}\text{Ne}$ , as an example. It is shown that the method gives a result identical to that calculated by the ordinary method using the two-body scattering solution.

The construction of this paper is as follows. In Sec. II A, we present the imaginary-time formalism for the radiative capture reaction rate. In Sec. II B, we discuss how the resonant and nonresonant contributions are included in our formalism. In Sec. III, our method is exemplified by applying it to the two-body capture reaction,  $^{16}\text{O}(\alpha, \gamma)^{20}\text{Ne}$ . In Sec. III A, we summarize radial equations to be employed in the practical calculation. In Sec. III B, we show results of the ordinary method's solution of the two-body scattering problem. We then compare the results of our method with those of the ordinary method in Sec. III C. Section IV is devoted to a summary.

## II. THEORY

### A. Imaginary-time method for radiative capture rate

We consider a radiative capture process of two or three nuclei confined in a large spatial area of volume  $V$ . The transition rate between nuclear states  $i$  and  $f$  accompanying an emission of a photon of multipolarity  $\lambda\mu$  is given by [12]

$$T_{fi}^{(\lambda\mu)} = \frac{8\pi(\lambda+1)}{\hbar\lambda[(2\lambda+1)!!]^2} \left(\frac{E_\gamma}{\hbar c}\right)^{2\lambda+1} |\langle\Psi_f|M_{\lambda\mu}|\Psi_i\rangle|^2, \quad (1)$$

where  $M_{\lambda\mu}$  is a transition operator. The energy of emitted photon  $E_\gamma$  is equal to the energy difference of two states,  $E_\gamma = E_i - E_f$ . The initial and final wave functions,  $\Psi_i$  and  $\Psi_f$ , are many-body wave functions. The initial state  $\Psi_i$  is a scattering state in which  $i$  specifies the relative momentum of colliding nuclei and other quantum numbers. The final state  $\Psi_f$  is a bound-state wave function after emitting the photon.

For two-body collisions, the transition rate in a unit spatial area and in a unit time under unit number densities of colliding nuclei is given by  $VT_{fi}^{(\lambda\mu)}$  and is equal to  $v\sigma_{fi}$ , where  $v$  is the relative velocity and  $\sigma_{fi}$  is the cross section. For three-body collisions, the reaction rate in a unit spatial area and in a unit time is given by  $V^2T_{fi}^{(\lambda\mu)}$ .

We denote the inverse temperature as  $\beta = 1/k_B T$  and express the thermonuclear reaction rate at the inverse temperature  $\beta$  as  $r(\beta)$ . This is related to the transition rate  $T_{fi}^{(\lambda\mu)}$  by

$$r(\beta) = \frac{\sum_{M_f\mu} \sum_i e^{-\beta E_i} V^{N-1} T_{fi}^{(\lambda\mu)}}{\sum_i e^{-\beta E_i}}, \quad (2)$$

where  $N = 2$  for two-body and  $N = 3$  for three-body collisions, respectively.  $M_f$  indicates the magnetic quantum number of final state  $f$ . The denominator is evaluated to be

$$\sum_i e^{-\beta E_i} \rightarrow \omega_i \frac{V^{N-1} \mu^{3/2}}{(2\pi\beta\hbar^2)^{3(N-1)/2}}, \quad (3)$$

where  $\mu$  is the reduced mass,  $\mu = m_1 m_2 / (m_1 + m_2)$  for the two-body case and  $\mu = m_1 m_2 m_3 / (m_1 + m_2 + m_3)$  for the three-body case, and  $\omega_i$  accounts for the degeneracy of the initial state.

An essential trick that brings us an imaginary-time evolution formula for the reaction rate is employment of the spectral representation of the Hamiltonian. Let  $f(\hat{H})$  be a certain function of the Hamiltonian operator  $\hat{H}$ . We then have

$$f(\hat{H}) = \sum_{n \in \text{bound}} f(E_n) |\Phi_n\rangle \langle \Phi_n| + \sum_{i \in \text{scattering}} f(E_i) |\Phi_i\rangle \langle \Phi_i|, \quad (4)$$

where  $E_n$  and  $\Phi_n$  are energy eigenvalues and eigenfunctions of bound states and  $E_i$  and  $\Phi_i$  are those of scattering states. For a general many-body Hamiltonian  $\hat{H}$ , the scattering states  $\Phi_i$  may include a variety of channels with different decompositions into fragments. For a two-body scattering state, the energy  $E_i$  is given by  $E_i = \hbar^2 k^2 / 2\mu$ , where  $k$  specifies the relative wave number of colliding nuclei. To take into account collisions of nuclei in excited states, we need to include the excitation energy in  $E_i$ .

Employing Eq. (4) with  $f(x) = e^{-\beta x} (x - E_f)^{2\lambda+1}$ , one may rewrite Eq. (2) as

$$r(\beta) = \frac{1}{\omega_i} \left(\frac{2\pi\beta\hbar^2}{\mu}\right)^{3/2} \frac{8\pi(\lambda+1)}{\hbar\lambda[(2\lambda+1)!!]^2} \times \sum_{M_f\mu} \langle\Psi_f|M_{\lambda\mu} e^{-\beta\hat{H}} \left(\frac{\hat{H} - E_f}{\hbar c}\right)^{2\lambda+1} \hat{P} M_{\lambda\mu}^\dagger |\Psi_f\rangle, \quad (5)$$

where  $\hat{P}$  is a projector to remove bound states,

$$\hat{P} = 1 - \sum_{n \in \text{bound}} |\Phi_n\rangle \langle \Phi_n|. \quad (6)$$

Equation (5) is the principal result of this paper. We find that the initial scattering states are removed in this expression.

For a practical calculation of Eq. (5), we introduce a wave function  $\Psi_{\lambda\mu,f}(\beta)$  by

$$\Psi_{\lambda\mu,f}(\beta) = e^{-\beta\hat{H}} \left(\frac{\hat{H} - E_f}{\hbar c}\right)^{2\lambda+1} \hat{P} M_{\lambda\mu}^\dagger \Psi_f. \quad (7)$$

Then the reaction rate is expressed as

$$r(\beta) = \frac{1}{\omega_i} \left(\frac{2\pi\beta\hbar^2}{\mu}\right)^{3/2} \frac{8\pi(\lambda+1)}{\hbar\lambda[(2\lambda+1)!!]^2} \times \sum_{M_f\mu} \langle\Psi_f|M_{\lambda\mu}|\Psi_{\lambda\mu,f}(\beta)\rangle. \quad (8)$$

The wave function  $\Psi_{\lambda\mu,f}(\beta)$  satisfies a time-dependent Schrödinger equation along the imaginary-time axis,

$$-\frac{\partial}{\partial\beta} \Psi_{\lambda\mu,f}(\beta) = \hat{H} \Psi_{\lambda\mu,f}(\beta), \quad (10)$$

with the initial condition,

$$\Psi_{\lambda\mu,f}(0) = \left(\frac{\hat{H} - E_f}{\hbar c}\right)^{2\lambda+1} \hat{P} M_{\lambda\mu}^\dagger \Psi_f. \quad (11)$$

In practical calculations, we repeat evolutions with a small imaginary-time step  $\Delta\beta$  to achieve a finite evolution,

$$\Psi_{\lambda\mu,f}(n\Delta\beta) = \hat{P} e^{-\Delta\beta\hat{H}} \hat{P} \dots \hat{P} e^{-\Delta\beta\hat{H}} \Psi_{\lambda\mu,f}(0). \quad (12)$$

The operation of the evolution operator with a small imaginary-time step,  $e^{-\Delta\beta\hat{H}}$ , may be achieved with the Taylor expansion method,

$$\Psi_{\lambda\mu,f}(\beta + \Delta\beta) = \hat{P} e^{-\Delta\beta\hat{H}} \Psi_{\lambda\mu,f}(\beta) \simeq \hat{P} \sum_{k=0}^N \frac{(-\Delta\beta\hat{H})^k}{k!} \Psi_{\lambda\mu,f}(\beta). \quad (13)$$

In an analytic expression, the projector  $\hat{P}$  is necessary only once in Eq. (5), since the Hamiltonian  $\hat{H}$  commutes with the projector  $\hat{P}$ . In practical calculations, however, it is indispensable to apply the projector at each step of Eq. (13).

### B. Resonant and nonresonant contributions

In the ordinary treatment of radiative capture processes, contributions of sharp resonances are treated separately from the nonresonant contribution. For a two-body collision, a contribution of the resonance of energy  $E_R$  and width  $\Gamma$  to the reaction rate is given by [1]

$$r_R(\beta) = \left(\frac{2\pi\beta}{\mu}\right)^{3/2} \hbar^2 \omega_R \frac{\Gamma_i \Gamma_f}{\Gamma} e^{-\beta E_R}, \quad (14)$$

where  $\Gamma_i$  and  $\Gamma_f$  are partial widths of the resonance to the initial channel through barrier penetration and to the final state through  $\gamma$  emission.  $\omega_R$  is the statistical factor given by

$$\omega_R = \frac{2J_R + 1}{(2I_1 + 1)(2I_2 + 1)}, \quad (15)$$

where  $J_R$  is the spin of the resonance and  $I_{1(2)}$  is the spin of colliding nucleus 1 (2).

Equation (5) includes both resonant and nonresonant contributions since all the final states are summed up. To confirm that resonant contribution is included in Eq. (5), we show that the resonant contribution  $r_R(\beta)$  may be extracted from it.

We assume that the partial decay width for  $\gamma$  emission,  $\Gamma_f$ , is much smaller than the partial width for binary or ternary decay through Coulomb barrier,  $\Gamma_i$ . Indeed, this is the condition that we may start with the transition rate expression of Eq. (2) in perturbation theory. We thus assume that the partial width decaying into the initial channel,  $\Gamma_i$ , almost exhausts the total width,  $\Gamma \simeq \Gamma_i$ . For a sharp resonance, we may express the resonant state by a normalized wave function  $\Phi_R$ . To calculate the resonant contribution, we replace the projector  $\hat{P}$  in Eq. (5) with the projector of the resonant state,  $|\Phi_R\rangle\langle\Phi_R|$ . Then we find the contribution of the resonant state may be expressed as

$$r(\beta; \Phi_R) = \frac{1}{\omega_i} \left(\frac{2\pi\beta\hbar^2}{\mu}\right)^{3/2} \frac{8\pi(\lambda+1)}{\hbar\lambda[(2\lambda+1)!!]^2} e^{-\beta E_R} \times \left(\frac{E_R - E_f}{\hbar c}\right)^{2\lambda+1} \sum_{M_f \mu M_R} |\langle\Psi_f|M_{\lambda\mu}|\Phi_R\rangle|^2, \quad (16)$$

where  $M_R$  specifies a magnetic substate of the resonance. Noting that the perturbation theory gives an expression for the radiative decay width of the resonant state  $\Phi_R$  as

$$\frac{\Gamma_f}{\hbar} = \frac{8\pi(\lambda+1)}{\hbar\lambda[(2\lambda+1)!!]^2} \left(\frac{E_R - E_f}{\hbar c}\right)^{2\lambda+1} \quad (17)$$

$$\times \sum_{M_f \mu} |\langle\Psi_f|M_{\lambda\mu}|\Phi_R\rangle|^2, \quad (18)$$

we arrive at the following result:

$$r(\beta; \Phi_R) = \omega_R \left(\frac{2\pi\beta\hbar^2}{\mu}\right)^{3/2} e^{-\beta E_R} \frac{\Gamma_f}{\hbar}. \quad (19)$$

This is equal to  $r_R(\beta)$  if we assume  $\Gamma = \Gamma_i$  in Eq. (14).

In practical calculations, there are two options when a sharp resonance exists. One is to treat the resonant contribution

separately, employing Eq. (14) and removing the resonant contribution from the expression of Eq. (5) by adding the projector of the resonant state to the projector  $\hat{P}$ . The other is just to perform the imaginary-time calculation as it is, so that the resonant contribution is automatically included in Eq. (14).

## III. TEST CALCULATION: $^{16}\text{O}(\alpha, \gamma)^{20}\text{Ne}$ CAPTURE RATE

### A. A potential model and radial equations

The formalism presented in Sec. II is applicable to general many-body descriptions. In this section, we apply the method to a radiative capture process of two-body collision,  $^{16}\text{O}(\alpha, \gamma)^{20}\text{Ne}$ , ignoring internal structure of the colliding nuclei. This process has been investigated in the potential model [13] and in microscopic cluster models [14,15]

We assume a simple potential model for the initial  $\alpha$ - $^{16}\text{O}$  scattering state and for the final excited state of  $^{20}\text{Ne}$ . This potential model has been adopted in Ref. [13] and has been shown to describe the process reasonably.

Numerical calculations will be achieved in the partial wave expansion. We first summarize the formula in the partial wave expansion for an  $\alpha$ - $^{16}\text{O}$  collision. We introduce a radial wave function for the relative motion in the ordinary way. For bound states, we denote

$$\Psi(\mathbf{r}) = \frac{u_{nl}(r)}{r} Y_{lm}(\hat{\mathbf{r}}), \quad (20)$$

where  $n$  is the nodal quantum number. We assume a normalization relation  $\int dr |u_{nl}(r)|^2 = 1$  as usual. For scattering states, we denote the radial wave function of energy  $E$  as  $u_{El}(r)$ , for which we assume the following normalization in the asymptotic region:

$$u_{El}(r) \rightarrow \left(\frac{2\mu}{\pi\hbar^2 k}\right)^{1/2} \sin\left(kr - \frac{l\pi}{2} + \delta_l\right), \quad (21)$$

with  $E = \hbar^2 k^2 / 2\mu$ . Then, there follows the following completeness relation for each  $l$  value,

$$\sum_n u_{nl}(r)u_{nl}(r') + \int_0^\infty dE u_{El}(r)u_{El}(r') = \delta(r - r'). \quad (22)$$

In the ordinary method, we first calculate the cross section and then calculate the reaction rate by integrating the cross section with a Boltzmann weight and a photon phase space factor. Denoting the radial wave function of initial state by  $u_{El_i}^{(i)}(r)$  and that of final state by  $u_{n_f l_f}^{(f)}(r)$ , the reaction rate is given by

$$r(\beta) = \sum_{l_f l_i \lambda} \frac{2}{\hbar} \left(\frac{2\pi\hbar^2\beta}{\mu}\right)^{3/2} \frac{(\lambda+1)(2\lambda+1)}{\lambda[(2\lambda+1)!!]^2} \times e^2 \left\{ 2 \left(\frac{16}{20}\right)^\lambda + 8 \left(-\frac{4}{20}\right)^\lambda \right\}^2 \times (2l_i + 1) |l_i 0 \lambda_0| |l_f 0|^2 q_{l_i l_i}^{(\lambda)}(\beta), \quad (23)$$

where we introduced  $q_{l_f l_i}^{(\lambda)}(\beta)$  by

$$q_{l_f l_i}^{(\lambda)}(\beta) = \int_0^\infty dE e^{-\beta E} \left( \frac{E - E_f}{\hbar c} \right)^{2\lambda+1} \times \left( \int_0^\infty dr u_{n_f l_f}^{(f)}(r) r^\lambda u_{E l_i}^{(i)}(r) \right)^2. \quad (24)$$

In the imaginary-time method, we employ a spectral representation of the Hamiltonian to remove the scattering wave function  $u_{E l_i}^{(i)}(r)$ . The final expression written in terms of the radial wave function is given by

$$q_{l_f l_i}^{(\lambda)}(\beta) = \langle u_{n_f l_f}^{(f)} | r^\lambda e^{-\beta \hat{H}_i} \left( \frac{\hat{H}_i - E_f}{\hbar c} \right)^{2\lambda+1} \hat{P}_i r^\lambda | u_{n_f l_f}^{(f)} \rangle, \quad (25)$$

where  $\hat{H}_i$  is the radial Hamiltonian for the partial wave  $l_i$ . The  $\hat{P}_i$  is the radial projector to remove bound states of the partial wave  $l_i$ .

Introducing a radial wave function  $u_{l_f l_i}^{(\lambda)}(r, \beta)$  by

$$u_{l_f l_i}^{(\lambda)}(r, \beta) = e^{-\beta \hat{H}_i} \left( \frac{\hat{H}_i - E_f}{\hbar c} \right)^{2\lambda+1} \hat{P}_i r^\lambda u_{n_f l_f}^{(f)}(r), \quad (26)$$

the function  $q_{l_f l_i}^{(\lambda)}(\beta)$  is given by

$$q_{l_f l_i}^{(\lambda)}(\beta) = \langle u_{n_f l_f}^{(f)} | r^\lambda | u_{l_f l_i}^{(\lambda)}(r, \beta) \rangle. \quad (27)$$

The radiative capture reaction of  $^{16}\text{O}(\alpha, \gamma)^{20}\text{Ne}$  proceeds dominantly from the initial  $\alpha$ - $^{16}\text{O}$  scattering state with  $l_i = 0$  relative angular momentum to the final  $2^+$  state of  $^{20}\text{Ne}$  at the excitation energy of 1.63 MeV after emission of the  $E2$   $\gamma$  ray [13]. Since our purpose here is to show the applicability of our method, we concentrate on the calculation of this transition component. Namely, we consider the case of  $\lambda = 2, l_i = 0$ , and  $l_f = 2$ .

We assume a simple Woods-Saxon form for the  $\alpha$ - $^{16}\text{O}$  potential with a radius parameter  $R_0 = 2.72$  fm and a diffuseness parameter  $a = 0.85$  fm. The depth of the potential is chosen so that the energies of bound states are reproduced reasonably. The potential depth of  $l = 0$  channel is set to  $V_0 = -150.23$  MeV to reproduce the ground-state energy of  $^{20}\text{Ne}$  from the  $\alpha$ - $^{16}\text{O}$  threshold,  $-4.63$  MeV. The potential depth of  $l = 2$  channel is set to  $V_0 = -147.95$  MeV to reproduce the excitation energy of first  $2^+$  state of  $^{20}\text{Ne}$ , 1.63 MeV. As for the Coulomb potential, we use that of a homogeneously charged sphere of radius  $1.3 \times 16^{1/3}$  fm. There appear many bound states in this potential besides the physical states. They correspond to the Pauli-forbidden states of many-body wave function. We include all the bound states, both physical and Pauli-forbidden states, in the projection operator  $\hat{P}_i$ . The calculations shown are achieved with a radial grid of  $\Delta r = 0.1$  fm. The Runge-Kutta method is used to solve the radial equation from the origin and a simple five-point finite-difference formula is used in the imaginary-time evolution for the second-order derivative operator in  $\hat{H}_i$ .

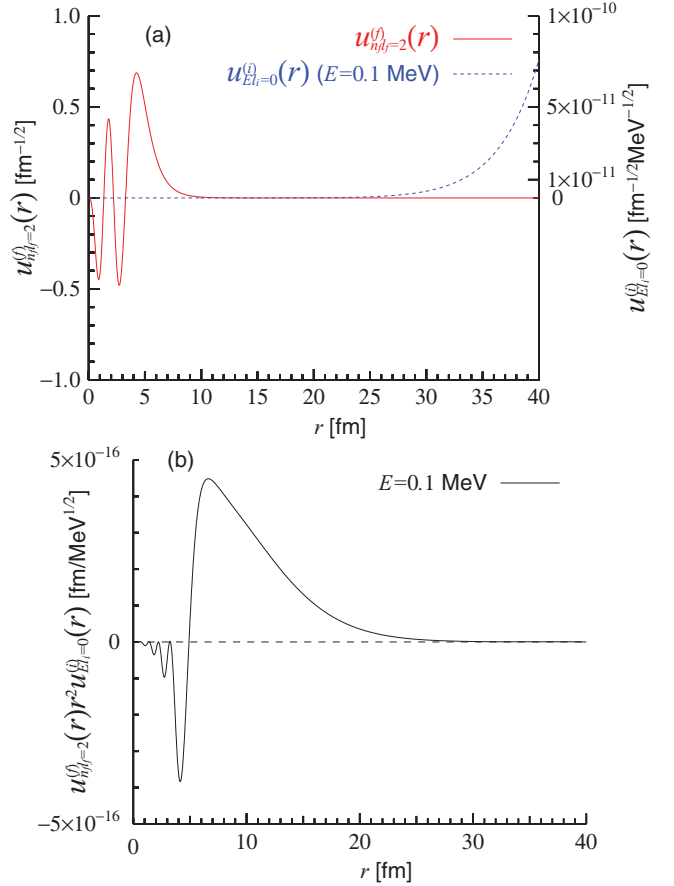


FIG. 1. (Color online) (a) The radial wave function of the initial scattering state,  $u_{E l_i}^{(i)}(r)$ , is shown for the incident relative energy  $E = 0.1$  MeV by the dotted curve, and the radial wave function of the final state,  $u_{n_f l_f}^{(f)}(r)$ , is shown by the solid curve. (b) The overlap function,  $u_{n_f l_f}^{(f)}(r) r^2 u_{E l_i}^{(i)}(r)$ , appearing in the integrand of Eq. (24) in the text.

## B. Ordinary method

Before showing results with the imaginary-time method, we first show calculations in the ordinary approach, solving the radial Schrödinger equation for each incident energy. Figure 1(a) shows the radial wave functions of initial and final states. The initial scattering wave,  $u_{E l_i}^{(i)}(r)$ , is shown by a dashed curve. The incident relative energy is set to  $E = 0.1$  MeV, which approximately corresponds to the Gamow window energy at  $T = 10^7$  K. The final bound-state wave function,  $u_{n_f l_f}^{(f)}(r)$ , is shown by a solid curve.

Figure 1(b) shows the integrand of the radial matrix element appearing in Eq. (24),  $u_{n_f l_f}^{(f)}(r) r^2 u_{E l_i}^{(i)}(r)$ . As seen from the figure, a dominant contribution comes from a spatial region where the final wave function  $u_{n_f l_f}^{(f)}(r)$  decays exponentially. We find the radial integration up to 30 fm in Eq. (24) is required to obtain a fully converged result.

We show in Fig. 2 the reaction rate  $q_{l_f=2, l_i=0}^{(\lambda=2)}(\beta)$  of Eq. (24) as a function of inverse temperature  $\beta = 1/k_B T$  by a solid line (left scale). We also show the Gamow energy as a function of inverse temperature by a dashed line (right scale). The inverse

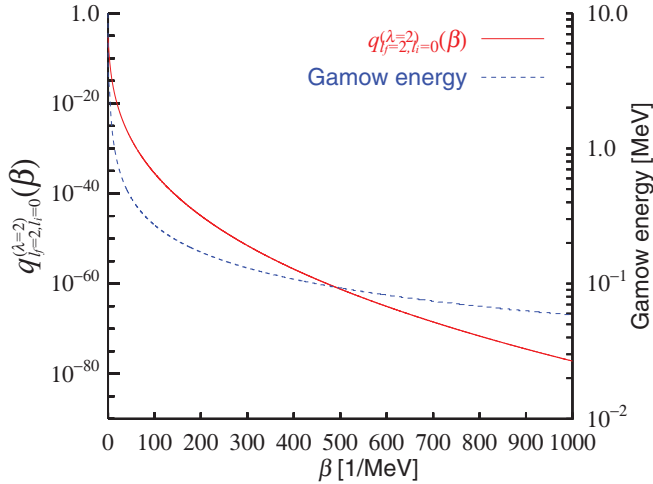


FIG. 2. (Color online) Solid curve and left scale: radiative capture reaction rate,  $q_{l_f=2, l_i=0}^{(\lambda=2)}(\beta)$ , calculated with the ordinary method of Eq. (24). Dashed curve and right scale: energy of Gamow window as a function of inverse temperature  $\beta$ .

temperature  $\beta = 10 \text{ MeV}^{-1}$  corresponds approximately to  $T = 1.1 \times 10^9 \text{ K}$  and  $\beta = 1000 \text{ MeV}^{-1}$  to  $T = 1.1 \times 10^7 \text{ K}$ .

### C. Imaginary-time method

We show in Fig. 3 the reaction rates,  $q_{l_f=2, l_i=0}^{(\lambda=2)}$ , calculated with the imaginary-time method. We find the calculated reaction rate depends on the radial region where the imaginary-time evolution is calculated. In Fig. 3, reaction rates calculated with different choices of radial cutoff distance  $R_{\text{max}}$  are compared. The reaction rate in the ordinary method, which was shown in Fig. 2, is also shown for comparison.

As is seen in the figure, the reaction rate falls off too rapidly if the radial cutoff distance is not sufficiently large.

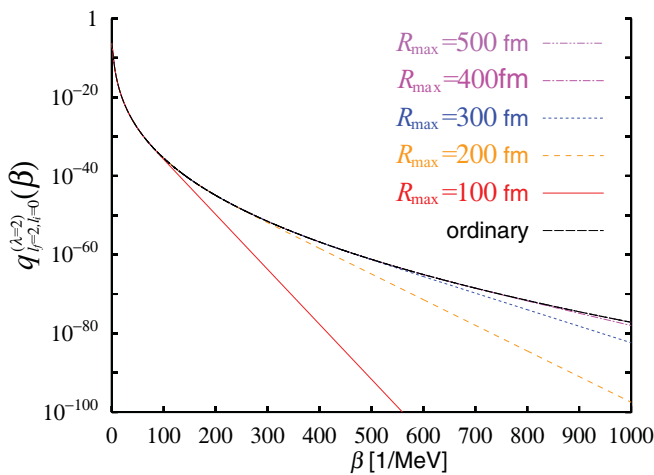


FIG. 3. (Color online) The radiative capture reaction rate  $q_{l_f=2, l_i=0}^{(\lambda=2)}$  calculated by the imaginary-time method of Eq. (25) is shown for several choices of radial cutoff distance  $R_{\text{max}}$ . For comparison, the reaction rate calculated with the ordinary method of Eq. (24) is also shown, which is denoted as “ordinary.”

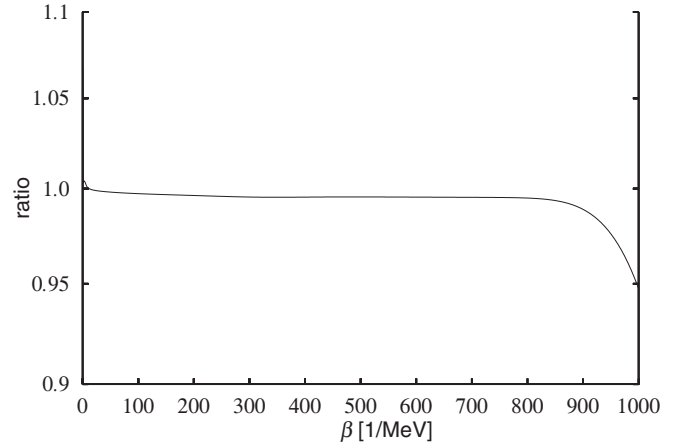


FIG. 4. The ratio of the reaction rate  $q_{l_f=2, l_i=0}^{(\lambda=2)}$  calculated by the imaginary-time method of Eq. (25) with  $R_{\text{max}} = 500 \text{ fm}$  to the reaction rate calculated with the ordinary method of Eq. (24).

The reaction rate calculated with the radial cutoff distance  $R_{\text{max}} = 500 \text{ fm}$  coincides almost completely with the reaction rate calculated in the ordinary method for a whole temperature region shown in the figure. In Fig. 4, we further show the ratio of the reaction rate calculated with  $R_{\text{max}} = 500 \text{ fm}$  to the reaction rate calculated in the ordinary method. One can again see that the imaginary-time method very accurately reproduces the result of the ordinary method. The discrepancy stays within an error of 1.2% for the region  $1 \text{ MeV}^{-1} < \beta < 900 \text{ MeV}^{-1}$ . We thus conclude that to obtain an accurate reaction rate at low temperature with the imaginary-time method, one needs to calculate the imaginary-time evolution of the wave function in a sufficiently large radial space, up to 500 fm for  $T \sim 10^7 \text{ K}$ .

Figure 3 indicates that the reaction rates by the imaginary-time method decrease exponentially at large  $\beta$  when the radial cutoff distance is not sufficiently large. We express the asymptotic behavior as  $q_{l_f=2, l_i=0}^{(\lambda=2)}(\beta) \simeq e^{-\beta\epsilon}$ , where the slope constant  $\epsilon$  depends on the radial cutoff distance,  $R_{\text{max}}$ . The  $\epsilon$  increases as the radial cutoff distance decreases. In the imaginary-time calculation, the wave function  $u_{l_f l_i}^{(\lambda)}(r, \beta)$  is dominated by the eigenfunction of the lowest eigenvalue when  $\beta$  is sufficiently large. Since all the bound states are removed in the imaginary-time evolution by the projection operator, the slope parameter  $\epsilon$  should coincide with the lowest positive energy eigenvalue of the Hamiltonian. Since the Coulomb potential decreases monotonically as a function of radial coordinate, the eigenfunction of the lowest positive eigenvalue should localize in the region close to the radial cutoff distance, if there is not a sharp resonant state below that energy.

In Fig. 5, we show the  $\alpha$ - $^{16}\text{O}$  potential and the eigenfunctions belonging to several positive low-energy eigenvalues. Calculation is achieved in the radial region up to  $R_{\text{max}} = 500 \text{ fm}$ . The  $\alpha$ - $^{16}\text{O}$  potential is composed of nuclear ( $V_N$ ) and Coulomb ( $V_C$ ) potentials, and the lowest positive-energy eigenvalue is close to the minimum of the Coulomb potential energy at the radial cutoff distance,  $E_{\text{min}} \sim Z_1 Z_2 e^2 / R_{\text{max}}$ .

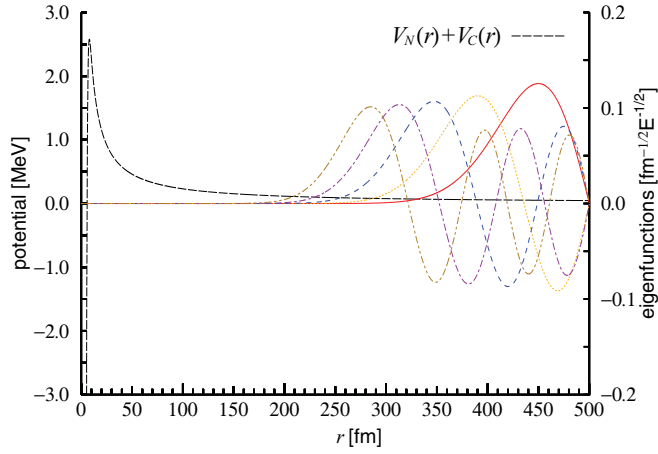


FIG. 5. (Color online) The  $\alpha$ - $^{16}\text{O}$  potential is denoted by a red solid curve (left scale). Five low positive-energy eigenfunctions of the potential are shown by dotted curves. Calculations are achieved in the radial region up to 500 fm.

For  $R_{\text{max}} = 500$  fm, the energy is  $E_{\text{min}} \sim 0.046$  MeV. For  $R_{\text{max}} = 100$  and 200 fm, the energies are  $E_{\text{min}} \sim 0.23$  and 0.115 MeV, respectively. These values explain the slope of the reaction rate at large  $\beta$  seen in Fig. 3.

It is evident that the imaginary-time evolution in the radial region inside a certain radial cutoff distance  $R_{\text{max}}$  takes into account only the tunneling process of energy higher than  $e^2 Z_1 Z_2 / R_{\text{max}}$ . As the temperature becomes lower, one needs to calculate the reaction rates in a wider radial region. We may estimate the radial cutoff distance  $R_{\text{max}}$  to obtain a reliable reaction rate for a given temperature  $\beta$  considering the energy of the Gamow window. Employing a standard formula for the peak energy of the Gamow window as a function of temperature and equating the energy with the Coulomb potential energy at the radial cutoff distance, we obtain

$$R_{\text{max}} \sim \left( \frac{2\hbar^2 Z_1 Z_2 e^2 \beta^2}{\mu \pi^2} \right)^{\frac{1}{3}}. \quad (28)$$

This gives  $R_{\text{max}} = 85$  fm for  $\beta = 10^2$  MeV $^{-1}$  and  $R_{\text{max}} = 394$  fm for  $\beta = 10^3$  MeV $^{-1}$ . This estimation coincides with the observation in Fig. 3 that the calculation up to  $R_{\text{max}} = 100$  fm describes the reaction rate for  $\beta < 100$  MeV $^{-1}$  and the calculation up to  $R_{\text{max}} = 500$  fm describes the rate for  $\beta < 1000$  fm.

For a deeper understanding of the imaginary-time method, we show in Figs. 6(a) and 6(b) the evolution of the radial wave function  $u_{l_f=2, l_i=0}^{(\lambda=2)}(r, \beta)$  in the imaginary time for several values of  $\beta$ . The calculation is achieved with  $R_{\text{max}} = 500$  fm. In the top four panels, the wave functions of  $\beta \leq 1$  MeV $^{-1}$  are shown in the linear scale. In the bottom panel, the absolute values of the wave functions are shown for large  $\beta$  values in the logarithmic scale.

To start the calculation, we prepare the radial wave function of the final state  $u_{n_f l_f=2}^{(f)}(r)$  inside a region,  $R_{\text{max}} = 30$  fm. In the top panel of Fig. 6(a), the wave function at  $\beta =$

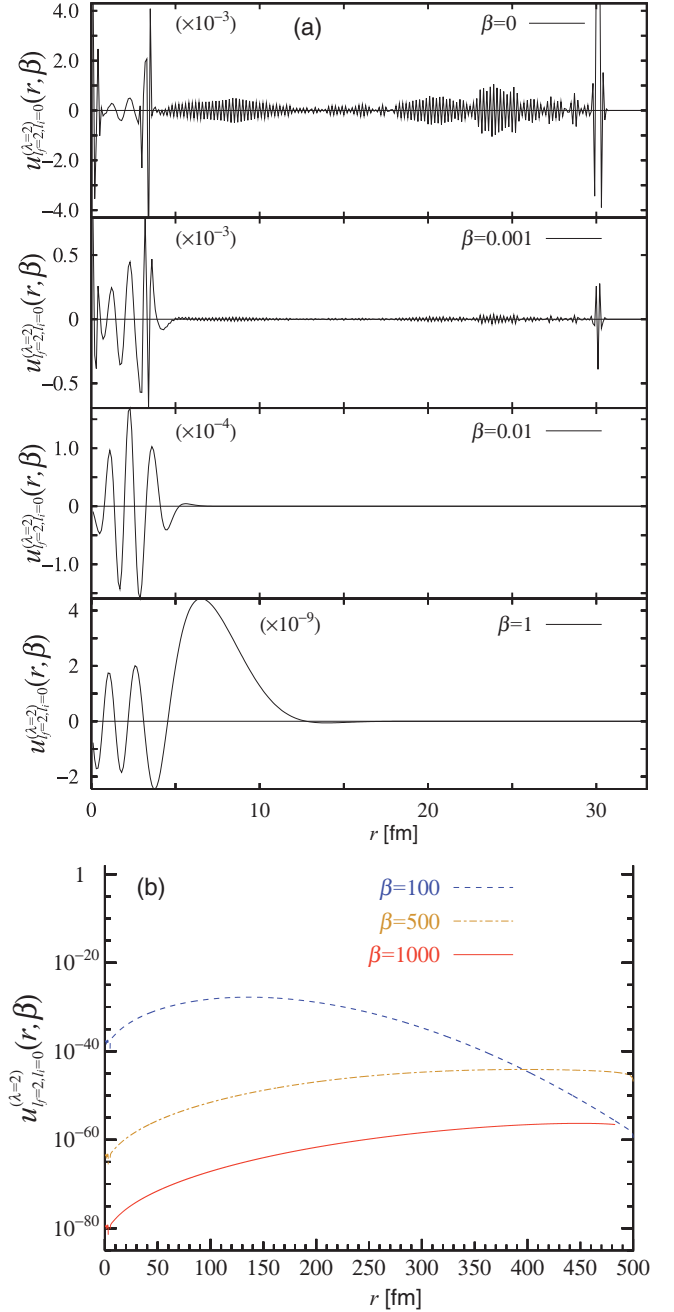


FIG. 6. (Color online) Imaginary-time evolution of the wave function as a function of radial coordinate  $r$ ,  $u_{l_f=2, l_i=0}^{(\lambda=2)}(r, \beta)$  defined by Eq. (26), (a) at  $\beta = 0, 0.001, 0.01,$  and  $1$  MeV $^{-1}$  in the linear scale and (b) at  $\beta = 100, 500,$  and  $1000$  MeV $^{-1}$  in the logarithmic scale.

0 is shown. We find a number of spikes in the initial wave function  $u_{l_f=2, l_i=0}^{(\lambda=2)}(r, \beta = 0)$ . In particular, an intense spike is seen at around  $r \simeq R_{\text{max}}^{(f)} = 30$  fm. These sharp structures originate from the operation of  $(\hat{H}_{l_i} - E_f)^5$  in preparing the wave function at  $\beta = 0$ . It works to emphasize components with high-energy eigenvalues of the radial Hamiltonian.

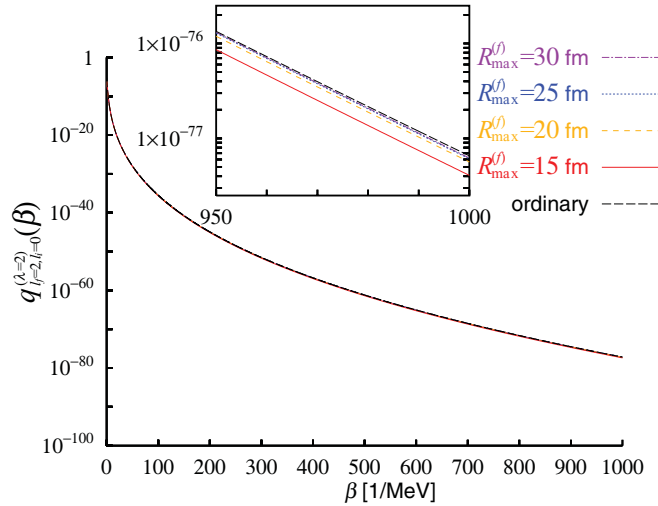


FIG. 7. (Color online) The dependence of the reaction rate  $q_{l_f=2, l_i=0}^{(\lambda=2)}(\beta)$  on the radial cutoff distance,  $R_{\max}^{(f)}$ , in preparing the final-state wave function  $u_{n_f l_f=2}^{(f)}(r)$ .

At first sight, the existence of such sharp structures looks unfavorable and problematic. However, these spikes disappear immediately after we start the imaginary-time evolution, and they will not affect the reaction rate at low temperature. Even at  $\beta = 0.001 \text{ MeV}^{-1}$ , these spikes are substantially reduced. They disappear almost completely at  $\beta = 0.01$ .

As the inverse temperature  $\beta$  increases, the wave function starts to shift outward. At  $\beta = 1 \text{ MeV}^{-1}$ , the amplitude of the wave function shows a peak at around 6 fm. As seen in Fig. 6(b), the dominant component of the wave function gradually shifts toward a region of large radial distance. Eventually, at  $\beta > 500 \text{ MeV}^{-1}$ , the radial wave function is dominated in the region of large radial distance. At  $\beta = 1000 \text{ MeV}^{-1}$ , the wave function of small radial region ( $r < 30 \text{ fm}$ ), which contributes to the radiative capture rate, is much smaller than that in the asymptotic region by an order of magnitude of about  $10^{20}$ . Thus, the imaginary-time calculation should be achieved with high accuracy to describe  $10^{20}$  difference of magnitude of the wave function in different radial regions.

To confirm that the result does not depend on the radial region in which we prepare the final wave function, we compare reaction rates employing final wave functions  $u_{n_f l_f}^{(f)}(r)$  prepared in the radial region with different cutoff radius,  $R_{\max}^{(f)}$ .

In Fig. 7, we compare reaction rates calculated by the imaginary-time method employing final wave functions of different radial cutoff distances,  $R_{\max}^{(f)}$ . We find the calculated reaction rate is quite insensitive to the radial cutoff distance. We thus confirm that a number of sharp structures seen in the top panel of Fig. 6(a), especially prominent at around the radial cutoff distance,  $R_{\max}^{(f)}$ , do not have any influence on the reaction rate calculation. As seen in the inset, the reaction rate is convergent if we choose  $R_{\max}^{(f)} \geq 25 \text{ fm}$ , which is consistent with our observation in Sec. III A.

We finally present a note on the dependence of the reaction rate on the choice of the nuclear potential in the imaginary-time

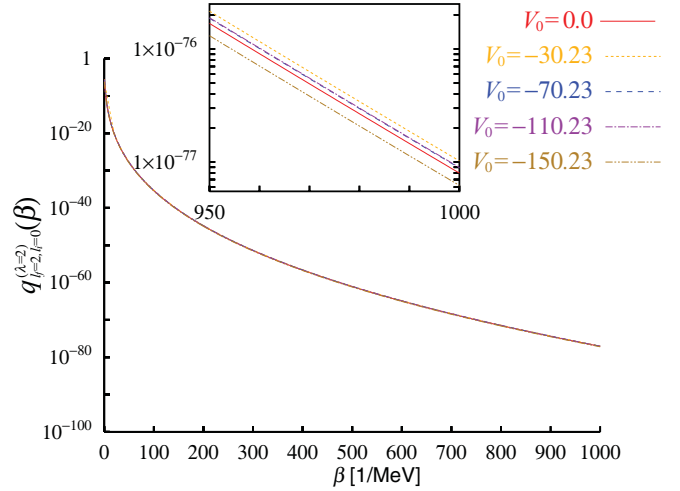


FIG. 8. (Color online) Reaction rates with different nuclear potential in the initial scattering channel are shown. The depths of the Woods-Saxon potential  $V_0$  is varied.

evolution. In Fig. 8, we compare the reaction rates changing the depths of the nuclear potential  $V_0$  of the Woods-Saxon potential in the initial scattering state with  $l_i = 0$ . All the other parameters are set to be the same. As seen from the figure, the reaction rate is quite insensitive to the choice of the parameter  $V_0$ . Even without the nuclear potential (i.e., with  $V_0 = 0$ ), the reaction rate is given almost correctly. As the inset shows, the difference is within a factor of 1.5 in  $950 \text{ MeV}^{-1} < \beta < 1000 \text{ MeV}^{-1}$ . We thus conclude that the nuclear potential in the initial channel, which will be used in the imaginary-time evolution, has very small effect on the reaction rate. Of course, this conclusion applies only to the nonresonant contribution. The resonance energy and width are sensitive to the nuclear potential, and so is the resonant contribution to the reaction rate.

#### IV. SUMMARY

In this paper, we proposed a new computational method for radiative capture reaction rate. Employing a spectral representation of the Hamiltonian, we have shown that the reaction rate as a function of temperature may be calculated without solving any scattering problem. Starting with an initial wave function that includes the final bound-state wave function after the emission of photon, the reaction rate as a function of inverse temperature,  $\beta (=1/k_B T)$ , can be obtained directly by solving a time-dependent Schrödinger equation in the imaginary-time axis.

To show the feasibility of the method, we show application of the method to  $^{16}\text{O}(\alpha, \gamma)^{20}\text{Ne}$  reaction in a simple potential model. We have confirmed that the new method gives an accurate reaction rate if we solve the imaginary-time evolution equation in a sufficiently large spatial area. Since the new method does not require any solution of scattering equation, it will be a promising approach for the reaction rate of triple- $\alpha$  radiative capture process. The application to that process is now in progress.

- [1] C. Angulo *et al.*, *Nucl. Phys. A* **656**, 3 (1999).
- [2] C. E. Rolfs and W. S. Rodney, *Cauldrons in the Cosmos* (University of Chicago Press, Chicago, 1988).
- [3] F. Hoyle, *Astrophys. J. Suppl.* **1**, 121 (1954).
- [4] C. W. Cook, W. A. Fowler, C. C. Lauritsen, and T. B. Lauritsen, *Phys. Rev.* **107**, 508 (1957).
- [5] K. Nomoto, F.-K. Thielemann, and S. Miyaji, *Astron. Astrophys.* **149**, 239 (1985).
- [6] K. Langanke, M. Wiescher, and F.-K. Thielemann, *Z. Phys. A* **324**, 147 (1986).
- [7] P. Descouvemont and D. Baye, *Phys. Rev. C* **36**, 54 (1987).
- [8] K. Ogata, M. Kan, and M. Kamimura, *Prog. Theor. Phys.* **122**, 1055 (2009).
- [9] M. Kamimura, M. Yahiro, Y. Iseri, Y. Sakuragi, H. Kameyama, and M. Kawai, *Prog. Theor. Phys. Suppl.* **89**, 1 (1986).
- [10] N. Austern, Y. Iseri, M. Kamimura, M. Kawai, G. H. Rawitscher, and M. Yahiro, *Phys. Rep.* **154**, 125 (1987).
- [11] R. de Diego, E. Garrido, D. V. Fedorov, and A. S. Jensen, *Phys. Lett. B* **695**, 324 (2011).
- [12] P. Ring and P. Schuck, *The Nuclear Many-Body Problem* (Springer-Verlag, New York, Berlin, Heidelberg, 1980).
- [13] P. Mohr, *Phys. Rev. C* **72**, 035803 (2005).
- [14] P. Descouvemont and D. Baye, *Phys. Lett. B* **127**, 286 (1983).
- [15] K. Langanke, *Z. Phys. A* **317**, 325 (1984).